ADVANCED MATERIALS INTERFACES
www.advmatinterfaces.de

Nanointerface-Driven Reversible Hydrogen Storage in the Nanoconfined Li–N–H System

Brandon C. Wood, Vitalie Stavila,* Natchapol Poonyayant, Tae Wook Heo, Keith G. Ray, Leonard E. Klebanoff, Terrence J. Udovic, Jonathan R. I. Lee, Natee Angboonpong, Joshua D. Sugar, and Pasit Pakawatpanurut*

Dedicated to Natchapol "Golf" Poonyayant, who died tragically at the age of 25 during the writing of this paper. Golf's interest in nanoconfined materials inspired this work, and he performed the experimental synthesis and much of the analysis. The world has lost a talented young man, and we have lost a dear friend.

Hydrogen is an excellent energy carrier, yet the development of lightweight solid-state materials for compact, low-pressure storage remains challenging.[1] Nanoconfinement can improve the hydrogen-storage viability of complex metal hydrides, with enhancements typically attributed to shortened diffusion pathways or surface-driven stability changes.[2,3] However, the equally important role of internal interfaces in these nanoconfined hydrides remains largely unexplored. Here, it is shown how these internal "nanointerfaces" within the high-capacity $Li_3N/[LiNH_2 + 2LiH]$ system can be leveraged to directly alter the pathways for hydrogenation and dehydrogenation upon nanoconfinement. The suppression of undesirable intermediate phases dramatically improves kinetics and lowers the thermodynamic requirements to achieve full reversibility. The results establish the importance of nanointerfaces in solid-state hydrogen-storage reactions and introduce a new paradigm for enhancing performance by engineering internal microstructure.

Dr. B. C. Wood, Dr. T. W. Heo, Dr. K. G. Ray, Dr. J. R. I. Lee
Lawrence Livermore National Laboratory
Livermore, CA 94551, USA
E-mail: brandonwood@llnl.gov
Dr. V. Stavila, Dr. L. E. Klebanoff, Dr. J. D. Sugar
Sandia National Laboratories
Livermore, CA 94551, USA
E-mail: vnstavi@sandia.gov
N. Poonyayant, N. Angboonpong, Prof. P. Pakawatpanurut
Center for Sustainable Energy and Green Materials
Center of Excellence for Innovation in Chemistry
and Department of Chemistry
Mahidol University
Bangkok 10400, Thailand
Dr. T. J. Udovic
National Institute of Standards and Technology
Gaithersburg, MD 20899, USA

DOI: 10.1002/admi.201600803

For more than a decade, $LiNH_2$ has been investigated as a potential material for lightweight and compact solid-state hydrogen storage, as it can participate in high-capacity reactions when combined with binary metal hydrides such as LiH[4–7] or MgH_2.[8] Chen et al.[4] first reported the hydrogen-storage performance of bulk α-Li_3N, which hydrogenates to $[LiNH_2 + 2LiH]$ via a two-step reaction pathway

$$\alpha\text{-}Li_3N + H_2 \Leftrightarrow Li_2NH + LiH \quad (1)$$

$$Li_2NH + LiH + H_2 \Leftrightarrow LiNH_2 + 2LiH \quad (2)$$

The combined sequence possesses a theoretical gravimetric density of 10.4 wt% H, and as written avoids the ammonia release associated with dehydrogenation of bulk $LiNH_2$.[5,6] It is well documented that the bulk material suffers from poor reaction kinetics.[9] Initial hydrogen release from the bulk $[LiNH_2 + 2LiH]$ mixture commences at ≈150 °C and reaches a maximum at ≈245 °C; however, the stability of the bulk intermediate $[Li_2NH + LiH]$ prevents further dehydrogenation until the temperature is raised to ≈430 °C.[6]

The precise microstructure during hydrogenation/dehydrogenation is difficult to determine since it depends on the conditions and progress of the reaction, and the constituent light elements are easily damaged by electron beam probes (Supporting Information). Nevertheless, a sensible rendering of the microstructure evolution can be generated based on prior studies.[4,6,10–16] As shown in **Figure 1**, the nitrogen-containing phases likely form a core–shell structure with contiguous, mobile $LiNH_2/Li_2NH$ and Li_2NH/Li_3N interfaces. The lattice contiguity of these N-containing phases is suggested by crystallographic similarities between $LiNH_2$ and Li_2NH pointed out by David et al.,[10] and by the high formation energies and diffusion barriers for NH_x defects in $LiNH_2$ and Li_2NH that inhibit the possibility of N interdiffusion.[11] In addition, the inference of nonstoichiometric Li/H compositions (i.e., $Li_{1+x}NH_{2-x}$) within the $LiNH_2$ and Li_2NH parent phases,[10,12,13] combined

ADVANCED MATERIALS INTERFACES
www.advmatinterfaces.de

ADVANCED SCIENCE NEWS
www.advancedsciencenews.com

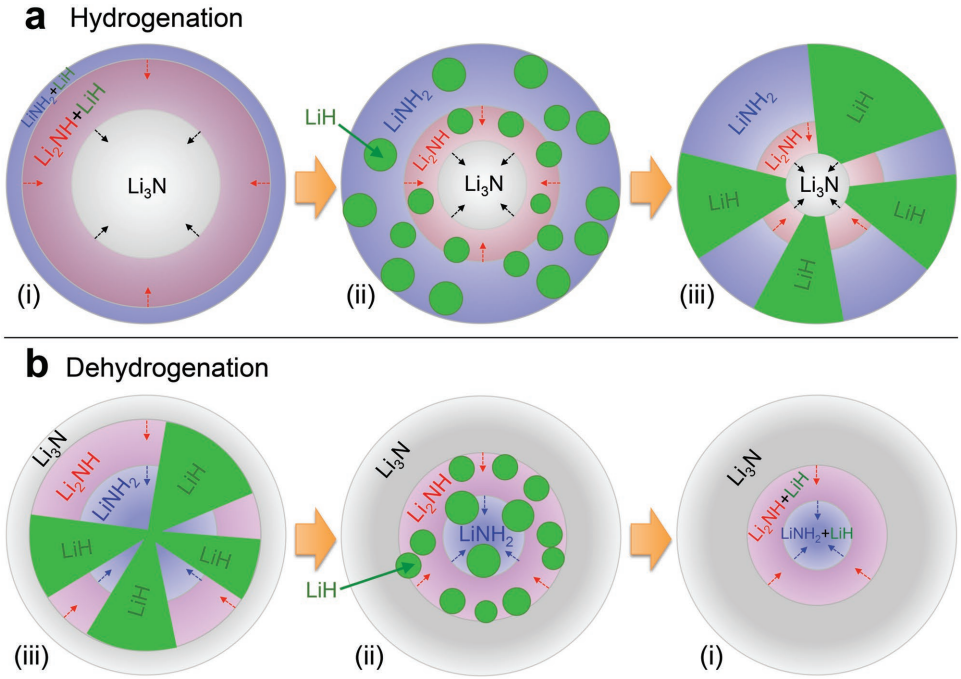

Figure 1. Schematic microstructure of the [$LiNH_2$+2LiH]/[Li_2NH+LiH]/Li_3N system. Panels (a) and (b) indicate Hydrogenation and dehydrogenation, respectively. The nitrogen-containing phases (blue = $LiNH_2$, pink = Li_2NH, gray = Li_3N) form a contiguous core–shell structure with phase boundaries propagating along the directions indicated by small arrows. a) During hydrogenation, LiH (green) is assumed to evolve from (i) a dispersed molecular, cluster, or solid-solution state to (ii) nucleated crystallites that eventually (iii) coarsen. b) Dehydrogenation follows the reverse pathway. Smaller particles favor the dispersed LiH state (i) due to interfacial penalties associated with nucleation.

with the predicted facile interdiffusion of Li and H,[10,14] suggest that Li and H compositions within the N-containing phases vary continuously along oppositely oriented chemical potential gradients. During hydrogenation, outer regions of the particle that are exposed to H_2 gas will therefore tend to be H-rich and Li-lean, and vice versa during dehydrogenation. The core–shell model microstructure in Figure 1 is generally consistent with previously proposed models.[17]

One can further assume that LiH appears throughout the Li_2NH and $LiNH_2$ phases. During initial hydrogenation (Figure 1a), LiH should begin in an embryonic state with dimers or clusters in a solid solution or nonstoichiometric mixture[13] (panel (i)). Multiple crystallites will then nucleate and grow along the reaction front (panel (ii)) before finally coarsening (panel (iii)). Dehydrogenation follows the reverse pathway (Figure 1b). This process ensures continuous, direct contact of LiH with the other phases, which is necessary for its involvement at every reaction stage (assuming no formation of highly diffusive intermediates); it also minimizes the diffusion pathways for Li and H exchange, which can occur locally across the LiH/Li_2NH and LiH/$LiNH_2$ phase boundaries in accordance with the surface defect creation mechanisms proposed by Hoang et al.[11,15] Other authors have similarly concluded that direct contact between LiH and $LiNH_2$ is probable for ball-milled systems.[4,6,14,16] The coexistence of LiH and nitrogen-containing phases[18] near the surface is further consistent with the observation of mixed isotopes as products of [$LiNH_2$ + 2LiD] dehydrogenation in the studies of Chen et al.[6]

Figure 1 highlights the variety of internal solid–solid "nanointerfaces" present during hydrogenation/dehydrogenation. The free-energy penalties associated with these phase boundaries will be proportionately more severe for nanoparticles. For instance, one can reasonably assume that nucleation of LiH crystallites within small nanoparticles (panels (ii) and (iii)) will be suppressed in favor of dispersed embryonic clusters (panel (i)) to reduce interfaces. Among other advantages, this should improve sluggish kinetics associated with decomposition of stable LiH crystallites.[19] We show here that the collective interfacial free-energy penalties have additional profound energetic consequences for phase stability, and are ultimately responsible for altering pathways and promoting reversibility in nanoconfined [$LiNH_2$ + 2LiH]/Li_3N. This new role of nanoconfinement in complex metal hydrides contrasts with better-established roles, such as kinetic improvements via shortened diffusion pathways and changes in phase stability due to surface energy effects.[3,4]

Changes in hydrogenation kinetics of Li_3N upon confinement were first reported by Demir-Cakan et al.,[20] who showed that enhancements could be achieved with Li_3N derived from decomposition of lithium azide in mesoporous carbon. However, the explosive nature of the decomposition introduces synthetic safety risks upon scale-up and could potentially damage the structural integrity of the nanoscaffold. Instead, we base our investigation on a new and improved synthetic route that involves dissolution of metallic lithium in liquid ammonia,[21] followed by the infiltration of the $Li(NH_3)_x$ solution into a nanoporous carbon (npC) host. Subsequent evaporation of ammonia from the solvated complexes results in formation of nanoconfined $LiNH_2$@npC, which forms Li_3N@npC when heated in vacuum at 340 °C. The overall sequence can be written:

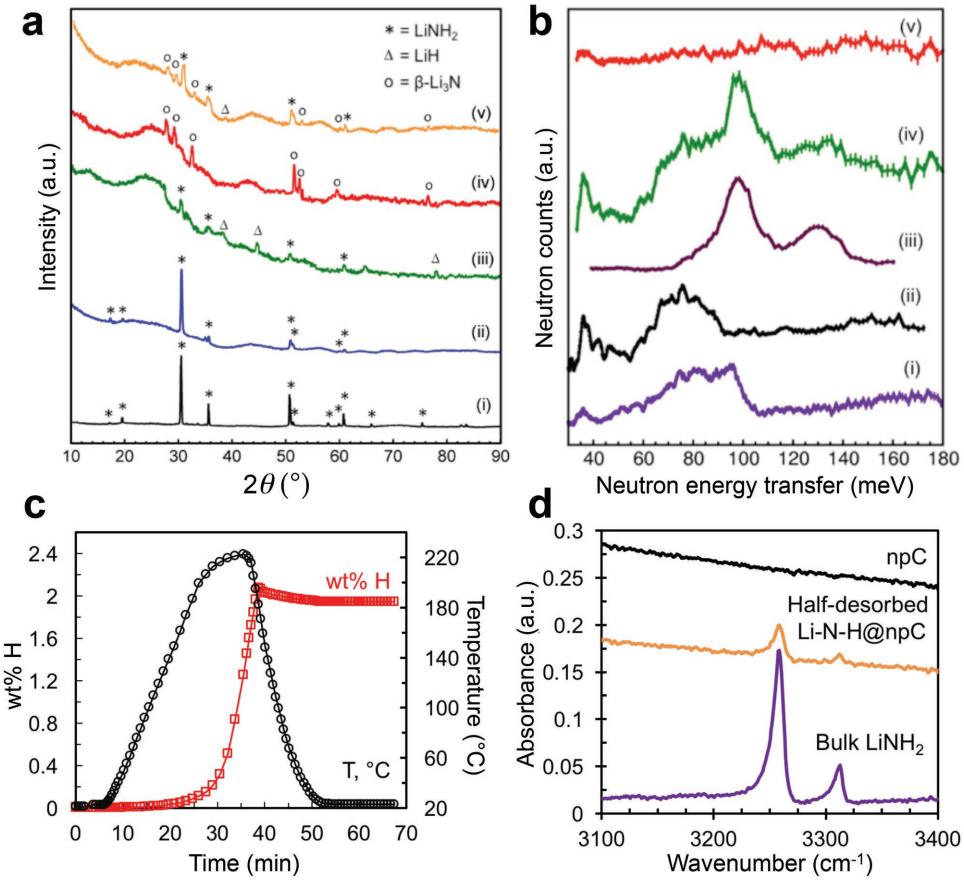

Figure 2. Characterization of reaction products. a) PXRD patterns of (i) bulk $LiNH_2$; (ii) as-synthesized nanoconfined $LiNH_2$@npC; and the synthesized material cycled at 250 °C ending in (iii) hydrogenated, (iv) dehydrogenated, and (v) half-dehydrogenated states. Crystalline phases are indicated by symbols: (*) for $LiNH_2$, (Δ) for LiH, and (o) for β-Li_3N. b) NVS at –269 °C for reference samples of (i) Li_2NH, (ii) $LiNH_2$, (iii) LiH, and the synthesized cycled material ending in (iv) hydrogenated and (v) dehydrogenated states. c) Sieverts and d) FTIR data for half-dehydrogenated $LiNH_2$@npC. In (d), FTIR data for empty npC and a bulk reference sample of authentic $LiNH_2$ are shown for comparison; these are shifted vertically for clarity of presentation but have not been scaled.

[Li (s) + NH_3 (l)]@npC → $Li(NH_3)_x$@npC → $LiNH_2$@npC → Li_3N@npC (see the Experimental Section). We used a npC host with an average pore size of 3.2 nm from porosimetry analysis (Figure S1, Supporting Information) and a Li_3N loading of 39.2 wt% from elemental analysis (Table S1, Supporting Information). **Figure 2**a shows powder X-ray diffraction (PXRD) for the as-synthesized $LiNH_2$@npC (Figure 2a(ii)) before conversion to Li_3N@npC. Comparison with the reference pattern for bulk $LiNH_2$ (Figure 2a(i)) confirms that $LiNH_2$ is the only crystalline phase present. Porosimetry measurements indicate a large decrease in the surface area and pore volume of npC upon infiltration, confirming that the active material is indeed inserted inside the nanopores (see the Supporting Information and Figures S2 and S3, Supporting Information).

The as-synthesized $LiNH_2$@npC material was heated to 340 °C in a Sieverts apparatus and then subjected to hydrogen cycling at temperatures up to 250 °C. Fully reversible hydrogenation/dehydrogenation was observed (**Figure 3**) with uptake of ≈4 wt% H relative to the mass of the sample, that is, including the mass of the inert npC scaffold. This translates to the active material cycling reversibly at ≈10.3 wt% H, consistent with the theoretical capacity of complete interconversion between [$LiNH_2$ + 2LiH] and Li_3N. Moreover, the nanoconfined [$LiNH_2$ + 2LiH]@npC material exhibited almost no capacity loss after five reversible cycles, indicating irreversible ammonia release associated with bulk $LiNH_2$ decomposition[22] was suppressed (further confirmed by mass spectrometry; see Figure S4, Supporting Information). Elemental analysis of the hydrogenated and dehydrogenated materials indicated compositions of $Li_{3.00}N_{1.01}H_{3.87}$ and $Li_{3.00}N_{1.03}$, respectively, very close to expected ratios for [$LiNH_2$ + 2LiH] and Li_3N (Table S1, Supporting Information). The PXRD patterns (Figure 2a) and neutron vibrational spectra (NVS; Figure 2b) of the material following hydrogenation (Figure 2a(iii),(iv)) and dehydrogenation (Figure 2a(iv)–(v)) further confirm that cycling between crystalline [$LiNH_2$ + 2LiH] and Li_3N is complete (note that NVS is dominated by H-derived vibrational modes and is sensitive to noncrystalline phases). Interestingly, the exclusive presence of $LiNH_2$ and LiH following hydrogenation means that the material has self-optimized upon thermal cycling, converting the as-synthesized $LiNH_2$@npC to the high-capacity [$LiNH_2$ + 2LiH]/Li_3N@npC system.

Hydrogen cycling of [$LiNH_2$ + 2LiH]/Li_3N@npC (Figure 3a) shows smooth absorption/desorption curves without

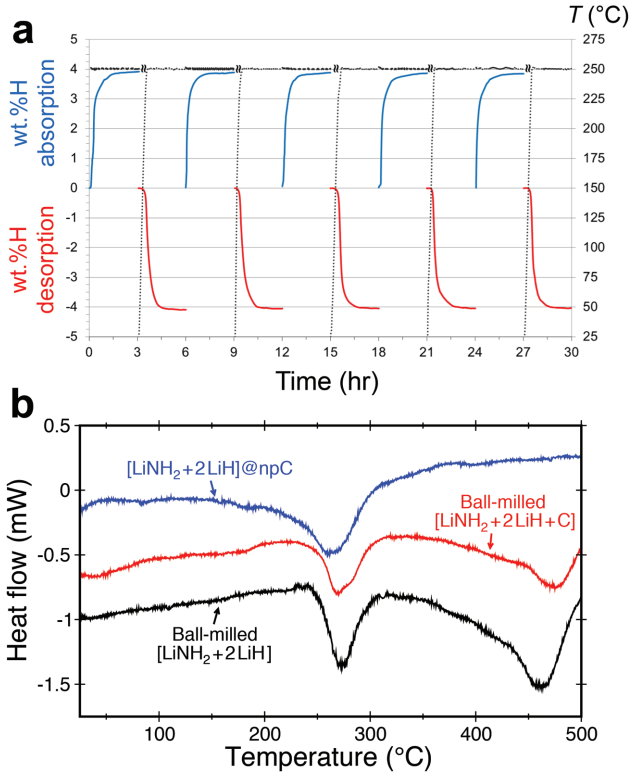

Figure 3. Reversible hydrogen capacity and single-step reaction pathway of nanoconfined $[LiNH_2+2LiH]/Li_3N$. a) Five consecutive absorption/desorption cycles of $[LiNH_2 +2LiH]$@npC at 250 °C with the temperature profiles shown by black dashed lines. Absorption was performed at 100 bar H_2 pressure. The sample was cooled to room temperature before subsequent desorption (this process is omitted for clarity). The reported material wt% H is relative to the sample mass, including the inert npC. b) DSC of $[LiNH_2+2LiH]$@npC (blue), showing a single-step pathway compared with the two-step pathway of ball-milled $[LiNH_2+2LiH]$ (black). DSC for a ball-milled mixture $[LiNH_2+2LiH+C]$ with graphite at an equivalent mass ratio to that of $[LiNH_2+2LiH]$@npC is shown in red. For clarity, curves for $[LiNH_2+2LiH+C]$ and $[LiNH_2+2LiH]$ are shifted by −0.5 and −1.0 mW, respectively.

intermediate plateaus, pointing to a single rate-limiting step in lieu of the two-step sequence observed for the bulk system.[4–6,19] The elimination of the second rate-limiting step is also seen in differential scanning calorimetry (DSC; Figure 3b), where the results indicate that kinetic limitations ordinarily associated with Li_2NH decomposition are no longer relevant after nanoconfinement. This strongly suggests that Li_2NH never appears as an isolable intermediate phase and that the reaction proceeds rapidly to Li_3N within a single rate-limiting step. The temperature for the initial onset of hydrogen release is also significantly lowered (≈150 °C) for the nanoconfined sample even without catalyst addition. To exclude effects of any secondary chemical interaction with the confinement medium, DSC data were also obtained for bulk $[LiNH_2 + 2LiH]$ ball-milled in the presence of graphite with a mass ratio equivalent to the nanoconfined sample. Results reproduced the two-step mechanism of the bulk system, confirming that the influence of the nanoconfining medium is physical rather than chemical in origin.

Furthermore, there is no evidence of any residual Li_2NH intermediate (peaks at 30.45°, 51.14°, and 60.92°)[23] in the PXRD patterns at the hydrogenated (Figure 2a(iii)) or dehydrogenated (Figure 2a(iv)) ends after cycling at 250 °C, despite the fact that this temperature is well within the stability range of bulk $[Li_2NH + LiH]$.[6] Similarly, NVS measurements confirm that the hydrogenated system can be expressed as a graphical convolution of only the reference $LiNH_2$ and LiH spectra, and that no trace of Li_2NH is seen upon subsequent dehydrogenation to Li_3N@npC (Figure 2b(v)). Fourier transform infrared spectroscopy (FTIR) was used to investigate intermediate stages of dehydrogenation. Figure 2c shows a Sieverts desorption and corresponding FTIR data for $[Li_2NH + LiH]$@npC interrupted at ~2 wt% hydrogen (i.e., half dehydrogenation). Only $LiNH_2$ is present, with no evidence for Li_2NH (strong absorption at 3100–3200 cm^{-1}[6]). The PXRD pattern of the half-dehydrogenated sample (Figure 2a(v)) likewise indicates that $LiNH_2$ and β-Li_3N are the major species (along with a trace amount of LiH). These data conclusively demonstrate direct dehydrogenation of $[LiNH_2 + 2LiH]$@npC to Li_3N@npC, in agreement with Figure 2. As additional evidence that nanoconfinement incurs changes in phase stability, the PXRD patterns for Li_3N@npC also reveal exclusive expression of the high-pressure β-Li_3N phase over α-Li_3N, despite the absence of high-pressure synthetic methods and the greater stability of α-Li_3N in the bulk form under the experimental reaction conditions.[4]

The two primary nanoconfinement-induced changes—elimination of the Li_2NH intermediate phase and the α-Li_3N phase in favor of β-Li_3N—are also associated with significantly improved kinetics and reversibility with respect to the bulk counterpart. Hydrogenation of β-Li_3N@npC is especially accelerated, reaching half capacity in only 10 min under 100 bar H_2 at 250 °C. The result is a kinetically enhanced, fully reversible material that demonstrates among the highest reversible hydrogen capacity of any reported confined complex metal hydride.

The key role of nanointerfaces in altering the phase transformation pathway of $[LiNH_2 + 2LiH]$@npC is demonstrated using thermodynamic modeling based on density functional theory (DFT) that takes into account the microstructures in Figure 1 to predict the phase fractions of potential products for particles of varying sizes. In addition to temperature- and pressure-dependent bulk and surface energies, our models consider oft-neglected free energy contributions from the evolving solid–solid phase boundaries. These interfacial energies were approximated as a weighted average of constituent surface energies, borrowing a common empirical technique for estimating generic grain-boundary energies in polycrystalline materials when explicit knowledge of the evolving interface structures is lacking.[24] (This approximation was further justified by computations showing unaltered qualitative behavior upon variation of the relative free energy contributions of each interface; see the Experimental Section and Table S5, Supporting Information). The surface energies of each phase were weighted according to their relative prevalence within a Wulff construction, which partially accounts for the details of the atomistic structure by effectively averaging over all likely phase-boundary geometries and orientations (see the Experimental Section; Tables S2–S4 and Figure S5, Supporting Information).

First, we investigate the relative stability of α-Li_3N and β-Li_3N in the limit of full dehydrogenation. In this case, no internal

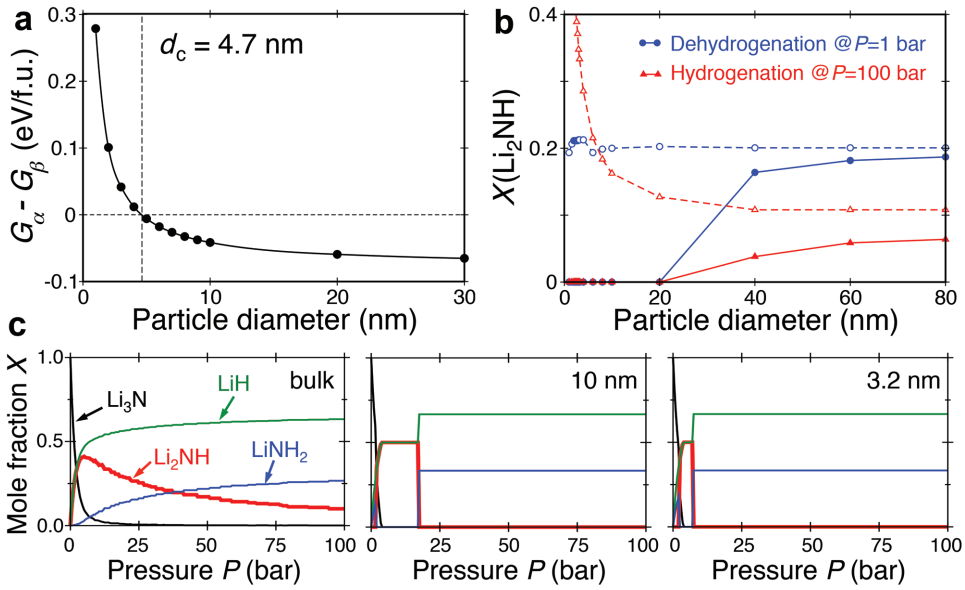

Figure 4. Predicted changes to the reaction pathway upon nanosizing. a) Calculated free energy difference (eV per formula unit) between α-Li_3N and β-Li_3N as a function of particle diameter (nm), showing a stability crossover at a critical diameter dc = 4.7 nm. b) Predicted equilibrium mole fraction X of Li_2NH following hydrogenation at P = 100 bar (red solid line) and dehydrogenation at P = 1 bar (blue solid line) as a function of particle diameter. Dashed lines are the equivalent results when interfacial free energy contributions are neglected. c) Predicted equilibrium mole fractions X of Li_3N (black), Li_2NH (red), $LiNH_2$ (blue), and LiH (green) as a function of H_2 pressure P (see the Experimental Section) upon isothermal hydrogenation of the bulk material (left) and particles of diameter d = 10 nm (center) and d = 3.2 nm (right). The schematic microstructure in panel (i) of Figure 1 is assumed. Predictions are generated at 727 °C using an ideal mixing model for phase coexistence (see the Experimental Section).

interfaces are present, and nanoparticle stability is determined exclusively by single-phase bulk and surface energetics. As shown in **Figure 4**a, β-Li_3N is indeed thermodynamically preferred over α-Li_3N for particle diameters < 4.7 nm, a direct consequence of the lower effective surface energy of β-Li_3N (0.66 J m^{-2}) versus α-Li_3N (0.73 J m^{-2}).

On the other hand, surface energies of individual phases are unable to account for the elimination of the Li_2NH phase that leads to a direct decomposition pathway; in fact, Li_2NH has one of the lowest surface energies among the various phases (Table S3, Supporting Information). Instead, it is necessary to consider the implications of the relevant solid–solid interfaces between other coexisting phases (Figure 1), whose interface areas and energies depend on microstructure and reaction progress.

For small nanoparticles, we can make simplifying assumptions concerning the evolution of the microstructure during (de)hydrogenation. In particular, dispersed embryonic LiH (Figure 1, panel (i)) will manifest during much of the reaction, since the critical nucleus diameter for LiH (computed to be ≥2.4 nm; see Figure S11 and the accompanying discussion, Supporting Information) represents a large volume fraction of smaller nanoparticles. LiH crystallites will therefore manifest only at near-complete hydrogenation conditions. Accordingly, we focus our discussion on the microstructures in panel (i) of Figure 1, although the other two reaction stages (LiH nucleation and coarsening) are considered in Figure S8 (Supporting Information) and lead to similar conclusions.

Figure 4b,c shows the equilibrium phase fraction behavior predicted by our models for different H_2 pressures mimicking (de)hydrogenation. These data are computed at 727 °C, which allows use of an ideal mixing model as a simplifying assumption to describe phase coexistence (see the Experimental Section; analogous results at 250 °C require implementation of a nonideal mixing model, which is explored in Figure S12, Supporting Information, and shows the same qualitative behavior). Figure 4b confirms that suppression of the Li_2NH intermediate phase becomes favorable at pressures relevant to hydrogenation (100 bar) and dehydrogenation (1 bar) for particles < 20 nm diameter. Moreover, the similarity in the hydrogenation and dehydrogenation pathways accounts for the reversibility of the $LiNH_2$ + 2LiH ⇔ β-Li_3N + $2H_2$ single-step reaction evidenced in Figure 3. Figure 4c shows the equilibrium phase fractions of Li_3N, Li_2NH, $LiNH_2$, and LiH predicted for hydrogenation as a function of pressure for three different particle sizes (bulk, d = 10 nm, and d = 3.2 nm). The pressure range for Li_2NH stability narrows as the particle size decreases, with the smallest particles (d = 3.2 nm) exhibiting an exceedingly thin stability range that disappears at H_2 pressures > 10 bar. Under nonequilibrium conditions, this regime will be quickly bypassed and the likelihood of nucleating Li_2NH will be negligible (Table S5, Supporting Information). This behavior explains the direct interconversion of Li_3N and [$LiNH_2$ + 2LiH] phases upon nanoconfinement. Larger particles, on the other hand, clearly express Li_2NH at intermediate stages in the reaction cycle. Parallel results for dehydrogenation showing the same Li_2NH phase suppression are provided in Figure S7 (Supporting Information).

Figure 4c also predicts higher phase purity after full cycling, in agreement with Figure 2: hydrogenation of the 3.2 nm diameter particle always gives an exact 2:1 LiH-to-$LiNH_2$ ratio, whereas conversion remains incomplete for the bulk material even at higher pressures. This tendency may explain why the

material self-optimizes to form [$LiNH_2$ + 2LiH]@npC upon initial cycling. Certain implications for improved kinetics can also be discerned. The phase fractions in Figure 4b transition much more abruptly at the nanoscale than in the bulk, suggesting a stronger driving force (and hence faster kinetics) for phase growth or depletion. Moreover, the elimination of Li_2NH as a solid phase necessarily increases the nonstoichiometric nature of $LiNH_2$ during intermediate reaction stages, which has been shown to enhance mass transport kinetics in the latter material (LiH suppression should also have a similar effect).[25]

To further establish that nanointerfaces drive the suppression of the Li_2NH intermediate phase, we computationally explored the sensitivity of the predicted phase fractions to contributions from the interface free energies. As expected, the penalizing effect of interfaces and surfaces is irrelevant in the bulk material but becomes increasingly severe as the particle size decreases (Figure S10, Supporting Information). Eventually, the Li_2NH phase is suppressed altogether in order to reduce the total number of interfaces within the nanoparticle, leading to direct hydrogenation and dehydrogenation. Moreover, nanoparticle simulations run without any interface contribution confirm that the presence of outer surfaces alone cannot account for the observed direct phase transformation pathway (Figure 4b). In addition to the spherical particle geometry in Figure 1, calculations were also performed on a rod-shaped geometry nanoconfined only in two dimensions, since such structures may reasonably exist within the npC framework due to the interconnectedness of pores. These results (Figure S9, Supporting Information) also generate sufficient nanointerface sensitivity to induce Li_2NH suppression and reaction reversibility, carrying practical consequences for particle morphology engineering.

Beyond demonstrating [$LiNH_2$ + 2LiH]/Li_3N@npC as a reversible, high-performing hydrogen-storage material, our work establishes that proper consideration of solid–solid nanointerfaces and particle microstructure is necessary for understanding hydrogen-induced phase transitions in complex metal hydrides. This highlights the analogy between hydrogen storage reactions and solid-state reactions in battery electrode materials, where internal interfaces have similarly been identified as important factors for altering phase transformation pathways.[26] Significantly, this introduces the possibility of tuning solid-state hydrogen-storage materials by tailoring morphology and internal microstructure, representing a new paradigm for engineering materials that could meet established performance targets. Further gravimetric capacity improvements may also be achieved using emerging encapsulants with higher theoretical surface areas and loading ratios.[4,27] Because nanointerface effects are amplified by the coexistence of multiple phases upon cycling, particularly prominent changes may be expected for nanoparticles with multicomponent mixtures.

Experimental Section

Synthesis of Li_3N@npC: Synthesis and handling of air-sensitive materials were carried out under an Ar atmosphere using standard Schlenk line and glove box techniques. For npC synthesis procedure and porosimetry measurements, see the Supporting Information. Synthesis of Li_3N@npC began with the synthesis of $LiNH_2$@npC. In a typical synthesis, 0.860 g of Li metal (99% pure from Aldrich) was placed in a Schlenk tube containing 3.109 g of activated npC. The tube was then suspended in a dry ice/acetone bath at −78 °C. Under continuous flow of Ar, anhydrous ammonia gas (ultrahigh purity, Matheson) was fed into the tube and condensed to form ≈20 mL liquid ammonia that completely covered the Li metal and npC. The mixture was stirred at −78 °C for 60 min to allow Li metal dissolution and infiltration, and the flask was left under a constant Ar flow so that liquid ammonia could slowly evaporate while the temperature gradually increased to room temperature for 16 h to yield $LiNH_2$@npC. This material was heated in vacuum at 340 °C to yield Li_3N@npC (through removal of NH_3 and H_2). Characterization details are given in Table S1 and Figures S1–S3 (Supporting Information).

DFT Calculations: DFT simulations were performed using Quantum Espresso[28] with ultrasoft pseudopotentials[29] based on the Perdew–Burke–Erzenhof exchange-correlation functional.[30] The plane-wave cutoff was 70 Ry and interatomic forces were converged to $<10^{-4}$ Ry $Å^{-1}$. Periodic bulk unit cells and internal coordinates for α-Li_3N (*P6/mmm*), β-Li_3N (*P6$_3$/mmc*), Li_2NH (*Fm-3m*), LiH (*Fm-3m*), and $LiNH_2$ (*I-4*) were relaxed to obtain zero-temperature lattice energies of formation E^{bulk} in good agreement with previous results[31] (see the Supporting Information and Table S2, Supporting Information, for relaxed cell parameters). Bulk free energies of formation were computed as E^{bulk} + ZPE − TS^{vib}, where ZPE is the zero-point energy and $-TS^{vib}$ is the phonon contribution to the vibrational free energy, calculated within the quasiharmonic approximation (Supporting Information and Table S4, Supporting Information). To obtain effective surface energies, total cleavage energies of the low-index surfaces s_i for each phase were first computed in a periodic slab geometry with 10 Å of vacuum according to $s_i = 1/2 \times (E(N) - N((E(N) - E(N–1))$, where $E(N)$ is the energy of an N-layer slab, with N chosen to generate slabs ≥ 1 nm thick. The Wulffman code[32] was used to obtain a Wulff construction for each phase. The effective surface energies s used in the thermodynamic calculations were computed as $s = A_s^{-1} \Sigma_i a_i s_i$, where A_s is the surface area of a sphere with volume equivalent to the Wulff-constructed particle, and a_i is the individual area of a facet. The free energy of H_2 was computed by adding finite-temperature contributions from the known equation of state[33] to a DFT-calculated reference total energy. For surface energies and Wulff constructions, see Table S3 and Figure S5 (Supporting Information).

Interface Energy Calculations: Interfacial energies γ_{ab} between phases a and b were estimated as $\gamma_{ab} = p\ (s_a + s_b)$, where s is the effective surface energy. This formula implicitly averages over all likely atomic arrangements and relaxes the assumption that crystallites are spherical, with different phase-boundary orientations and interface geometries instead expressed according to their statistical weight within the Wulff construction. For dispersed LiH (panel (i) in Figure 1), interfacial contributions were ignored. Plots in the main text were generated with $p = 0.5$; full robustness of the key conclusions against the precise choice of p was confirmed by independently varying p from 0.3 to 0.7 for each unique interface in the system (Table S5, Supporting Information).

Thermodynamic Phase-Fraction Calculations: The reversible reactions $-a \times [Li_3N+2H_2] \Leftrightarrow b \times [Li_2NH+LiH+H_2] \Leftrightarrow c \times [LiNH_2+2LiH]$ were considered, where a, b, and c define the reaction progress. Competing reactions involving intermediate ammonia formation were not considered, since ammonia is consumed quickly upon reaction with dispersed LiH[18,19,34] (its release is also suppressed in the experimental nanoconfined material; see Figure S4, Supporting Information). The Gibbs free energy G is expressed as a function of temperature T and H_2 pressure P_H as $G(T,P_H) = (n_S \times g_S) + (n_G \times g_G)$, where g_S and g_G are the molar contributions for n_S and n_G moles of solid and gas, respectively, expressed in terms of a, b, and c (Supporting Information). An ideal H_2 gas is assumed according to $g_G = g_G^0(T) + RT \ln(P_H/P_0)$, where $g_G^0(T)$ is the reference free energy of H_2 gas at the standard state (P_0 = 1 atm). For data in Figure 4, an ideal mixture of solid-phase fractions X_i according to $g_S = g_\gamma + \Sigma_i X_i \times [g_i^0(T) + RT \ln X_i]$ is also assumed (nonideal mixing is explored in the Supporting Information). The term g_γ includes the molar surface and interface contributions, which depend on the particle size and microstructural configuration (derivations of g_γ for the microstructures in Figure 1 are in the Supporting Information).

The free energies $g_i^0(T)$ of the individual pure solid components were computed from DFT, with the reference phase for Li_3N (α-Li_3N vs β-Li_3N) chosen according to the stability crossover criterion in Figure 4a. The X_i were computed by minimizing G with respect to a, b, and c under constraints associated with the corresponding microstructure (listed in Figure S6, Supporting Information).

All spherical core–shell geometries in Figure 1 and a rod-shaped geometry were tested to confirm robustness of the predicted size-dependent reaction pathway changes with respect to specific microstructure assumptions (Figures S6–S11, Supporting Information). The specific temperature for the isothermal plots in Figure 4 (727 °C) was selected to establish a suitable reference for which well-defined stability regimes for Li_3N, Li_2NH, and $LiNH_2$ were predicted in the bulk material, and full H_2 desorption was achieved. This allows us to unambiguously isolate size-dependent changes to the phase transformation pathway. Results for nonideal mixing with a larger activity coefficient at 250 °C are presented in Figure S12 (Supporting Information); however, since the activity coefficient introduces another unknown parameter, only ideal mixing results are presented in Figure 4 for clarity of presentation. Because pressure calibration in Figure 4c depends on temperature and does not account for nonequilibrium kinetics, attention should be drawn to the qualitative behavior of Li_2NH phase suppression and reversibility rather than quantitative transition pressures.

Supporting Information

Supporting Information is available from the Wiley Online Library or from the author.

Acknowledgements

The authors acknowledge support through the Hydrogen Storage Materials Advanced Research Consortium of the U.S. Department of Energy (DOE), Office of Energy Efficiency and Renewable Energy, Fuel Cell Technologies Office under Contract Nos. DE-AC52-07NA27344 and DE-AC04-94AL85000, as well as the Boeing Company via Boeing/Sandia CRADA SC02/1651.14.00. Part of the work was performed under the auspices of the DOE by Lawrence Livermore National Laboratory under Contract No. DE-AC52-07NA27344. Sandia National Laboratories is a multiprogram laboratory managed and operated by Sandia Corporation, a wholly owned subsidiary of Lockheed Martin Corporation, for the DOE's National Nuclear Security Administration under Contract No. DE-AC04-94AL85000.

Received: August 18, 2016
Revised: November 13, 2016
Published online:

[1] a) J. O. Keller, L. E. Klebanoff, S. Schoenung, M. Gillie, in *Hydrogen Storage Technology, Materials and Applications* (Ed: L. E. Klebanoff), Taylor and Francis, Boca Raton, FL **2012**, Ch. 1; b) S. Orimo, Y. Nakamori, J. R. Eliseo, A. Züttel, C. M. Jensen, *Chem. Rev.* **2007**, *107*, 4111.

[2] a) P. E. De Jongh, M. Allendorf, J. J. Vajo, C. Zlotea, *MRS Bull.* **2013**, *38*, 488; b) T. K. Nielsen, F. Besenbacher, T. R. Jensen, *Nanoscale* **2011**, *3*, 2086; c) J. J. Vajo, *Curr. Opin. Solid State Mater. Sci.* **2011**, *15*, 52; d) A. S. Arico, P. Bruce, B. Scrosati, J.-M. Tarascon, W. Van Schalkwijk, *Nat. Mater.* **2005**, *4*, 366; e) M. Fichtner, *Nanotechnology* **2009**, *20*, 204009; f) T. Mueller, G. Ceder, *ACS Nano* **2010**, *4*, 5647.

[3] L. Chong, X. Zeng, W. Ding, D.-J. Liu, J. Zou, *Adv. Mater.* **2015**, *27*, 5070.

[4] P. Chen, Z. Xiong, J. Luo, J. Lin, K. L. Tan, *Nature* **2002**, *420*, 302.

[5] T. Ichikawa, S. Isobe, N. Hanada, H. Fujii, *J. Alloys Compd.* **2004**, *365*, 271.

[6] P. Chen, Z. Xiong, J. Luo, J. Lin, K. L. Tan, *J. Phys. Chem. B* **2003**, *107*, 10967.

[7] T. Ichikawa, H. Y. Leng, S. Isobe, N. Hanada, H. Fujii, *J. Power Sources* **2006**, *159*, 126.

[8] W. Luo, S. Sickafoose, *J. Alloys Compd.* **2006**, *407*, 274.

[9] a) J. Wang, H.-W. Li, P. Chen, *MRS Bull.* **2013**, *38*, 480; b) H. Cao, Y. Zhang, J. Wang, Z. Xiong, G. Wu, P. Chen, *Prog. Nat. Sci. Mater. Int.* **2012**, *22*, 550; c) D. H. Gregory, *J. Mater. Chem.* **2008**, *18*, 2321.

[10] W. I. F. David, M. O. Jones, D. H. Gregory, C. M. Jewell, S. R. Johnson, A. Walton, P. P. Edwards, *J. Am. Chem. Soc.* **2007**, *129*, 1594.

[11] K. Hoang, A. Janotti, C. G. Van de Walle, *Phys. Rev. B* **2012**, *85*, 064115.

[12] J. W. Makepeace, M. O. Jones, S. K. Callear, P. P. Edwards, W. I. F. David, *Phys. Chem. Chem. Phys.* **2014**, *16*, 4061.

[13] A. Huq, J. W. Richardson, E. R. Maxey, D. Chandra, W.-M. Chien, *J. Phys. Chem. C* **2007**, *111*, 10712.

[14] K.-F. Aguey-Zinsou, J. Yao, Z. X. Guo, *J. Phys. Chem. B* **2007**, *111*, 12531.

[15] K. Hoang, A. Janotti, C. G. Van de Walle, *Angew. Chem.* **2011**, *123*, 10352.

[16] L. L. Shaw, R. Ren, T. Markmaitree, W. Osborn, *J. Alloys Compd.* **2008**, *448*, 263.

[17] a) L. L. Shaw, W. Osborn, T. Markmaitree, X. Wan, *J. Power Sources* **2008**, *177*, 500; b) T. Markmaitree, R. Ren, L. L. Shaw, *J. Phys. Chem. B* **2006**, *110*, 20710.

[18] W.-M. Chien, J. Lamb, D. Chandra, A. Huq, J. Richardson Jr., E. Maxey, *J. Alloys Compd.* **2007**, *446*, 363.

[19] J. Lamb, D. Chandra, W.-M. Chien, *J. Phys. Chem. C* **2011**, *115*, 14386.

[20] R. Demir-Cakan, W. S. Tang, A. Darwiche, R. Janot, *Energy Environ. Sci.* **2011**, *4*, 3625.

[21] J. J. Lagowski, *Pure Appl. Chem.* **1971**, *25*, 429.

[22] a) S. Isobe, T. Ichikawa, S. Hino, H. Fujii, *J. Phys. Chem. B* **2005**, *109*, 14855; b) H. Y. Leng, T. Ichikawa, S. Hino, N. Hanada, S. Isobe, H. Fuji, *J. Phys. Chem. B* **2004**, *108*, 8763.

[23] Y. Nakamori, A. Ninomiya, G. Kitahara, M. Aoki, T. Noritake, K. Miwa, Y. Kojima, S. Orimo, *J. Power Sources* **2006**, *155*, 447.

[24] D. A. Porter, K. E. Easterling, *Phase Transformations in Metals and Alloys*, 2nd ed., Chapman and Hall, London **1992**.

[25] B. Paik, M. Matsuo, T. Sato, L. Qu, A. R. Wolczyk, S.-I. Orimo, *Appl. Phys. Lett.* **2016**, *108*, 213903.

[26] M. Wagemaker, F. M. Mulder, A. Van der Ven, *Adv. Mater.* **2009**, *21*, 2703.

[27] E. S. Cho, A. M. Ruminski, S. Aloni, Y.-S. Liu, J. Guo, J. J. Urban, *Nat. Commun.* **2016**, *7*, 10804.

[28] P. Giannozzi, S. Baroni, N. Bonini, M. Calandra, R. Car, C. Cavazzoni, D. Ceresoli, G. L. Chiarotti, M. Cococcioni, I. Dabo, A. Dal Corso, S. de Gironcoli, S. Fabris, G. Fratesi, R. Gebauer, U. Gerstmann, C. Gougoussis, A. Kokalj, M. Lazzeri, L. Martin-Samos, M. Marzari, F. Mauri, R. Mazzarello, S. Paolini, A. Pasquarello, L. Paulatto, C. Sbraccia, S. Scandolo, G. Sclauzero, A. P. Seitsonen, A. Smogunov, P. Umari, R. M. Wentzcovitch, *J. Phys. Condens. Matter* **2009**, *21*, 395502.

[29] D. Vanderbilt, *Phys. Rev. B* **1990**, *41*, 7892.

[30] J. Perdew, K. Burke, M. Ernzerhof, *Phys. Rev. Lett.* **1996**, *77*, 3865.

[31] J. Herbst, L. Hector Jr., *Phys. Rev. B* **2005**, *72*, 125120.

[32] R. E. García, J. Blendell, Equilibrium Wulff Shape Generator, https://nanohub.org/resources/wulffman (accessed: February 2016).

[33] M. W. Chase Jr., *J. Phys. Chem. Ref. Data, Monogr.* **1998**, *9*, 1.

[34] T. Ichikawa, N. Hanada, S. Isobe, H. Y. Leng, H. Fujii, *J. Phys. Chem. B* **2004**, *108*, 7887.